

DOI: 10.1002/adem.201300454

Fabrication and Deformation of Metallic Glass Micro-Lattices**

By Jan Rys, Lorenzo Valdevit, Tobias A. Schaedler, Alan J. Jacobsen, William B. Carter and Julia R. Greer*

Recent progress in micro- and nanofabrication techniques enables the creation of hierarchically architected microlattices with dimensional control over six orders of magnitude, from centimeters down to nanometers. This hierarchical control facilitates the exploration of opportunities to exploit nano-sized material effects in structural materials. In this work, we present the fabrication, characterization, and properties of hollow metallic glass NiP microlattices. The wall thicknesses, deposited by electroless plating, were varied from ≈ 60 nm up to 600 nm, resulting in relative densities spanning from 0.02 to 0.2%. Uniaxial quasi-static compression tests revealed two different regimes in deformation: (i) Structures with a wall thickness above 150 nm failed by catastrophic failure at the nodes and fracture events at the struts, with significant micro-cracking and (ii) Lattices whose wall thickness was below 150 nm failed initially via buckling followed by significant plastic deformation rather than by post-elastic catastrophic fracture. This departure in deformation mechanism from brittle to deformable exhibited by the thin-walled structures is discussed in the framework of brittle-to-ductile transition emergent in nano-sized metallic glasses.

1. Introduction

Designing structural materials, which have both high strength and extended deformability, i.e. not suffering from catastrophic failure at room temperature, has been a subject of rigorous

pursuit. Such structures are well known from nature, for example the hierarchical architecture of the butterfly wing (Figure 1a–d). For decades, engineers have tried to emulate the design principles from nature and used cellular materials to fulfill highly specialized structural and multi-functional demands. These applications range from lightweight cores in payload fairings to impact protection for passenger transportation to enhanced surface areas in catalysts.^[1,2] Cellular materials can be produced as open- or closed-cell structures, with unit cells either ordered or randomly arranged. In contrast to stochastic foams, properly designed ordered lattices exhibit superior specific Young's modulus and strength.^[3] These benefits arise from a more efficient load transfer from the macro to the micro-scale, whereby lattice members deform primarily by axial stretching, as opposed to bending. This results, for example, in an improved scaling of the Young's modulus, E , with relative density, $\bar{\rho}$, from a second order power-law (Figure 1f) to linear.^[3] The overall mechanical properties of lattices are governed by the combination of structural response, dictated by the geometry, and by the microstructure and properties of the constituent material.^[4] Traditional fabrication techniques have been capable of producing structures down to the millimeter scale, with recent progress in micro and nano-fabrication enabling the expansion in the characteristic dimensions over six orders of magnitude, down to the nanometer scale.^[5,6] This size reduction facilitates exploring the opportunities to exploit nano-sized material effects in structural materials. An example of such a material size effect

[*] J. R. Greer

Division of Engineering and Applied Sciences, California Institute of Technology, Pasadena, CA 91106, USA
E-mail: jrgreer@caltech.edu

L. Valdevit

Department of Mechanical and Aerospace Engineering, University of California, Irvine, CA 92697, USA

T. A. Schaedler, A. J. Jacobsen, W. B. Carter

HRL Laboratories Limited Liability Company, Malibu, CA 90265, USA

J. Rys

Department of Materials, ETH Zurich, 8093 Zurich, Switzerland

[**] The authors gratefully acknowledge the financial support of DARPA through the Materials with Controlled Microstructural Architecture program and of JRG's NASA Early Career grants. The authors are grateful to Ramathasan Thevamaran and Ladan Salari for helping on bulk compression testing, Scott Godfrey for FE simulations, Lucas Meza and Dongchan Jang for fruitful discussions and the Kavli Nanoscience Institute (KNI) at Caltech for providing support and infrastructure.

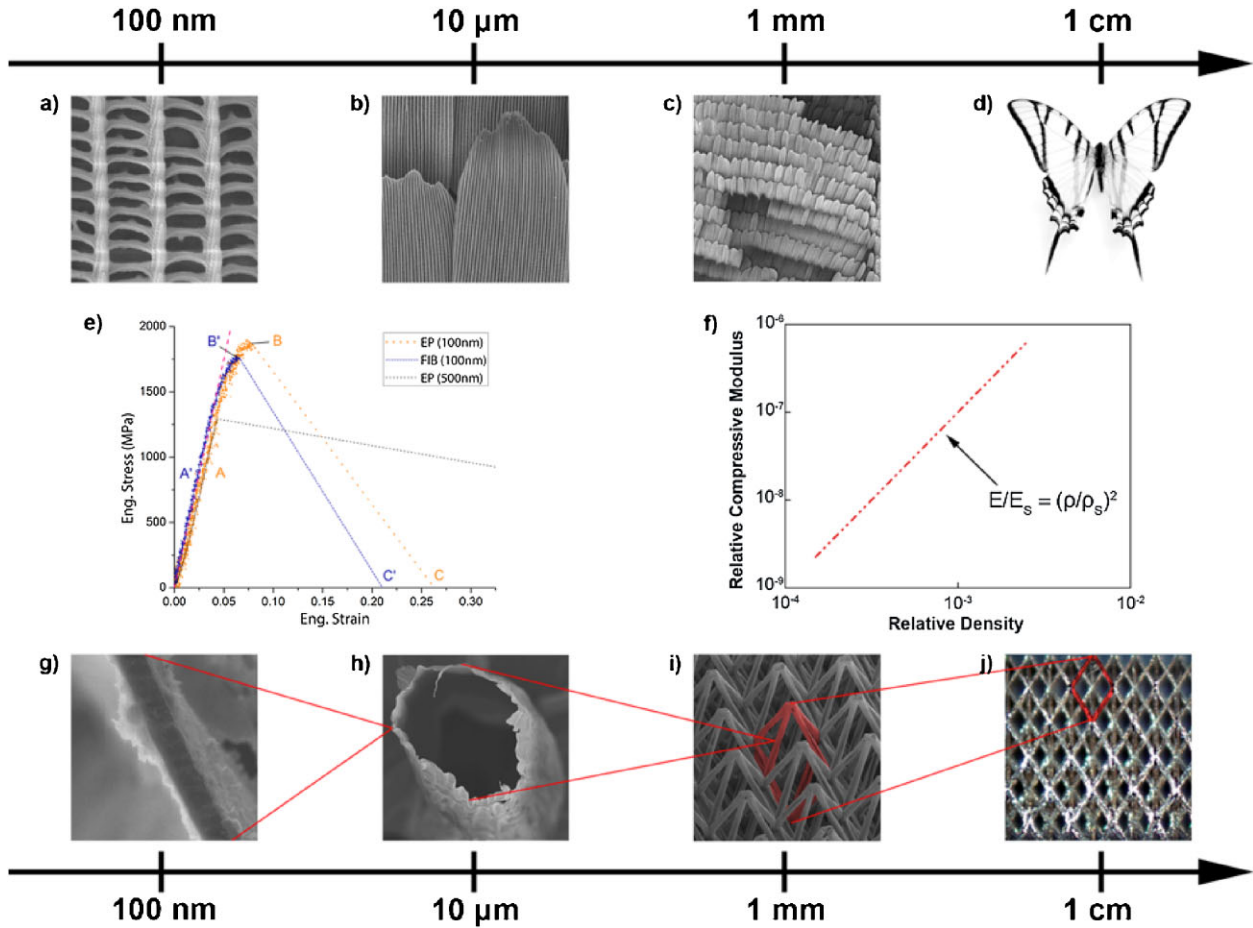


Fig. 1. Hierarchical design inspired by nature. (a–d) SEM images of a butterfly wing, showing the hierarchical design to the nanometer scale (Images are reprinted from ref^[42]). (g–j) open-cellular structure of an amorphous hollow NiP microlattice. (f) Theoretical $E \sim \rho^2$ scaling for stochastic open cellular foams.^[11] (e) Mechanical behavior of NiP metallic glass nanopillars with a wall thickness of 500 and 100 nm under tension.^[32]

is the emergence of brittle-to-ductile transition in the deformation of nanometer-sized metallic glasses, whose strengths typically range from ≈ 1.5 GPa to as high as 5 GPa.^[7–11] Reducing sample dimension below some critical value, typically 100 to 400 nm, has been reported to lead to a transition from a highly localized catastrophic failure mode to a homogeneous deformation behavior without sacrifice in tensile strength (Figure 1e).^[7–9,12,13]

We report the fabrication, characterization and properties of hollow amorphous nickel–phosphorous (Ni–P) microlattices with relative density, $\bar{\rho}$, defined as the density of the lattice, ρ , divided by that of the constituent solid, ρ_s , ranging from 0.2 to 0.02%. The sacrificial polymer pre-form was fabricated from an interconnected pattern of self-propagating photopolymer waveguides with characteristic dimensions spanning from micron to millimeter to centimeter scale (Figure 1g–i).^[6] Details on the polymer scaffold fabrication can be found in Jacobsen *et al.*^[6] A conformal amorphous film of NiP whose thickness ranged from ≈ 60 to 600 nm was deposited onto the polymer scaffold via electroless plating process. The polymer was subsequently removed, leaving a hollow Ni–P metallic glass microlattice shown in Figure 1j. Mechanical properties of these lattices were obtained by conducting uniaxial quasi-static

compression experiments. To gain further insights into the deformation mechanisms of these thin-walled structures, a single unit cell was compressed in situ in a custom-made nanomechanical instrument. Results indicate that the Ni–P metallic glass microlattices with relative densities below 0.5% attained roughly an order of magnitude higher maximum compressive strengths compared with the nanocrystalline NiP microlattices with similar geometry and characteristic dimensions.^[14] These thin-walled micro-lattices also did not suffer from catastrophic failure, unlike the thicker-walled counterparts. We attribute this advantageous combination of strength amplification and suppression of catastrophic failure to the microstructure-driven size effects in nano-sized materials and to the transition from brittle to ductile deformation mechanism in nano-metallic glasses. These results may provide a viable and economic route to design and fabricate high-strength, lightweight structural materials by combining structural effects (Figure 1f) with material size effects (Figure 1e).

2. Fabrication

We used a five-step wet chemistry process to fabricate the hollow metallic glass micro-lattices:^[14–21] (i) surface

Table 1. Bath composition for electroless plating of amorphous NiP.

Component	Quantity [g L ⁻¹]
Nickel(II) chloride hexahydrate	40
Sodium hypophosphite monohydrate	25
Succinic acid	50

modification, (ii) sensitization by absorption of Sn(II), (iii) catalysis via reduction of Pd(II), (iv) electroless deposition of nickel-based metallic glasses, and (v) removal of polymer template. The thiol-ene based polymer skeletons with truss-like architectures were created using a methodology similar to that described in Jacobsen *et al.*^[6] and were post-cured at 160 °C in N₂ environment for 24 h. To activate the surface for the chemisorption, the template was etched in an aqueous solution containing sulfuric and chromic acids (ratio 100:1 wt%). After thoroughly rinsing with water, the polymer structure was sensitized in an aqueous solution containing 0.3 g L⁻¹ stannous chloride and 0.3 mL L⁻¹ concentrated hydrochloric acid. Subsequent to a rinse with deionized water the polymer template was transferred into the catalyst solution containing palladium chloride and hydrochloric acid (premix RTM B from Transene Company, Inc) and rinsed with deionized water again. The deposition of Ni–P was performed at 87 ± 1 °C at a deposition rate of around 10 nm min⁻¹ using the formulation provided in Table 1. The resulting wall thicknesses ranged from 60 nm up to 600 nm. To remove the polymer template, the metallized sample was immersed for 24 h at 50 °C into a 1.5 M sodium hydroxide solution made of 50 vol% methanol and 50 vol% water. Samples with wall thicknesses below 150 nm were dried using a CO₂ critical point dryer (Automegasamdri[®]-915B from Tousimis) after replacing the sodium hydroxide solution with deionized water and then by filtered isopropyl alcohol to avoid wall collapse.

3. Microstructural Characterization

The microstructure of electroless deposited NiP films depends strongly on the phosphorous content. The film can be classified into three different types: low (<3 wt% P), medium

(4–7 wt% P) and high (>7 wt% P) phosphorus coatings.^[22–26] To analyze the microstructure, an 870 nm thick NiP film was deposited onto a 100 Si-wafer coated with a stack of 10 nm-thick layer of Ti and a 150–200 nm thick Au film both deposited using e-beam deposition. The Ti “sticking” layer served as an adhesion promoter. The NiP deposition was performed using the same parameters and bath composition as for the deposition onto the polymer template. Energy dispersive X-ray (EDX) analysis revealed the relative ratios of 85.2 wt% Ni and 14.8 wt% P, a composition in agreement with previously reported results.^[27] Figure 2a shows the X-ray diffraction (XRD) pattern for this Ni_{75.3}P_{24.7} film, using Cu Kα (λ = 1.540598 Å) radiation. The two sharp peaks at 2θ = 38° and 2θ = 69° correspond to Au(111) and Si(100), respectively. The broad peak in 2θ between 40° and 50° suggests that the Ni–P film was amorphous,^[28] which was verified by the dark-field transmission electron microscopy (TEM) image and the corresponding diffuse diffraction pattern of a 80 nm thick hollow tube (Figure 2b).

4. Nanoindentation

Young’s modulus of the Ni–P film was obtained via nanoindentation into a 620 nm-thick film, using a sharp Berkovich tip (TI 900 TriboIndenter, Hysitron). To minimize the contribution of the substrate to the overall measured Young’s modulus, the indentation was performed to a depth of 73 ± 4 nm, which represents ≈11% of the film thickness.^[29] Accounting for the compliance of the indenter tip, the Young’s modulus, *E_s*, was calculated to be 143 ± 8 GPa following the Oliver–Pharr method.^[30] The hardness, *H*, was measured to be 5.3 GPa and corresponds to an estimated yield strength, *σ_y*, of 1.77 GPa, using the approximation *σ_y* ≈ *H*/3 typically used for metals.^[31] These results are in good agreement with previously reported nanoindentation tests of amorphous NiP films^[27] and with tensile experiments on electroplated Ni–P metallic glass nanopillars.^[32]

5. Quasi-Static Compression Experiments

Quasi-static compression experiments at the lattice level were conducted using two different set-ups: (i) An Instron

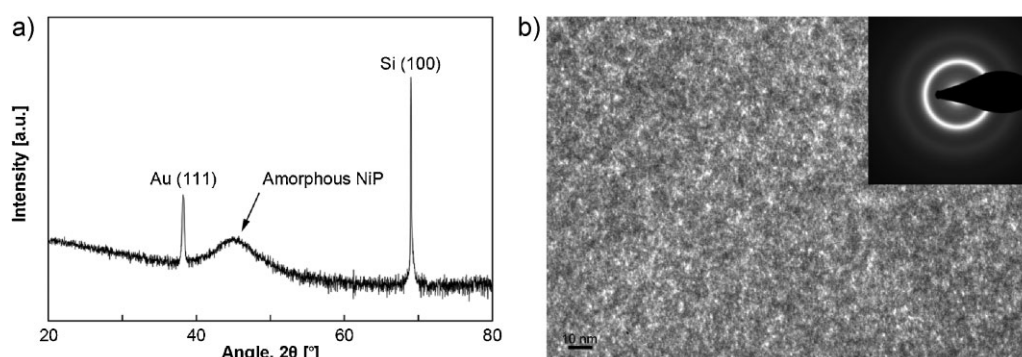


Fig. 2. Microstructural analysis of electroless deposited NiP films. (a) XRD analysis of an electroless NiP film deposited on a gold-coated silicon wafer. No other crystal peaks than Au(111) and Si(100) are present. (b) Dark field TEM of the wall of a 80 nm thick hollow tube. Inset shows the diffuse diffraction rings typical of an amorphous material.

E3000 frame equipped with a 250 N load cell (Instron) and (ii) an Instron 8862 frame equipped with a 2.5 N load cell (Honeywell). Figure 3a and b shows two sets of representative engineering stress versus strain curves for samples with wall thicknesses of 85 nm (Figure 3a) and 600 nm (Figure 3b), each loaded-and-unloaded three times to 25% strain and 50% strain, respectively. Both samples exhibited elastic loading over the first 2–4% strain followed by a peak in stress between 5 and 8% strain, which corresponds to the collapse of the top-most horizontal layer of unit cells, likely due to variations in the strut diameter at the surface of the microlattice. Following the initial peak, the stress dropped by a factor of ≈ 2 over the following 12% strain before it increased again. This suggests that the structure failed sequentially, with each lower layer buckling after the one above it was fully collapsed. During unloading, the stress decreased rapidly by $\approx 90\%$ over the initial 10% of unloading strain. The deformation of the 600 nm thick-walled samples was characterized by a plateau in stress over 4% strain before vanishing. This plateau was likely a result of the relaxation of the buckled and/or elastically deformed struts and remaining intact nodes. When unloaded-and-reloaded, the Young's modulus in these samples decreased by $\approx 93\%$ and the peak stress – by $\approx 75\%$. In contrast, the 85 nm thick-walled samples exhibited a more prominent plateau, extending over $\approx 15\%$ strain, followed by a nearly complete recovery, as well as a reduction in modulus by a factor of 2.7 and in the peak stress

by a factor of 2.5 upon second loading. This reduction in both the modulus and the peak stress suggests a correlation of these properties with wall thickness, with more permanent damage being accrued after the first loading cycle in the thick-walled samples. All subsequent cycles were nearly identical and added marginal additional damage to the structure.

Figure 3c and e shows the scanning electron microscopy (SEM) micrographs of the compressed samples with wall thicknesses of 95 nm (Figure 3c) and of 600 nm (Figure 3e). These images reveal that both samples collapsed via localized buckling at the nodes and along the struts. Post-mortem images of the 600 nm thick-walled sample illustrate the occurrence of catastrophic failure at the nodes and fracture events at the struts, with significant micro-cracking. The deformed regions were populated with numerous shear bands, indicated by the arrows in Figure 3e, as is typical for bulk metallic glasses.^[10] In contrast, the 95 nm thick-walled sample underwent a different deformation mechanism, with extensive buckling, micro-folding, and localized deformation (Figure 3c) The nodes and struts were not cracked and likely experienced high strains without failure. No evidence of shear banding or catastrophic micro-cracking could be detected.

Log-log plots of the relative compressive modulus, \bar{E} , and the maximum attained compressive stress, σ_{\max} , of the first cycle as a function of the relative density, $\bar{\rho}$, are presented in Figure 4. The relative modulus, \bar{E} , was calculated by

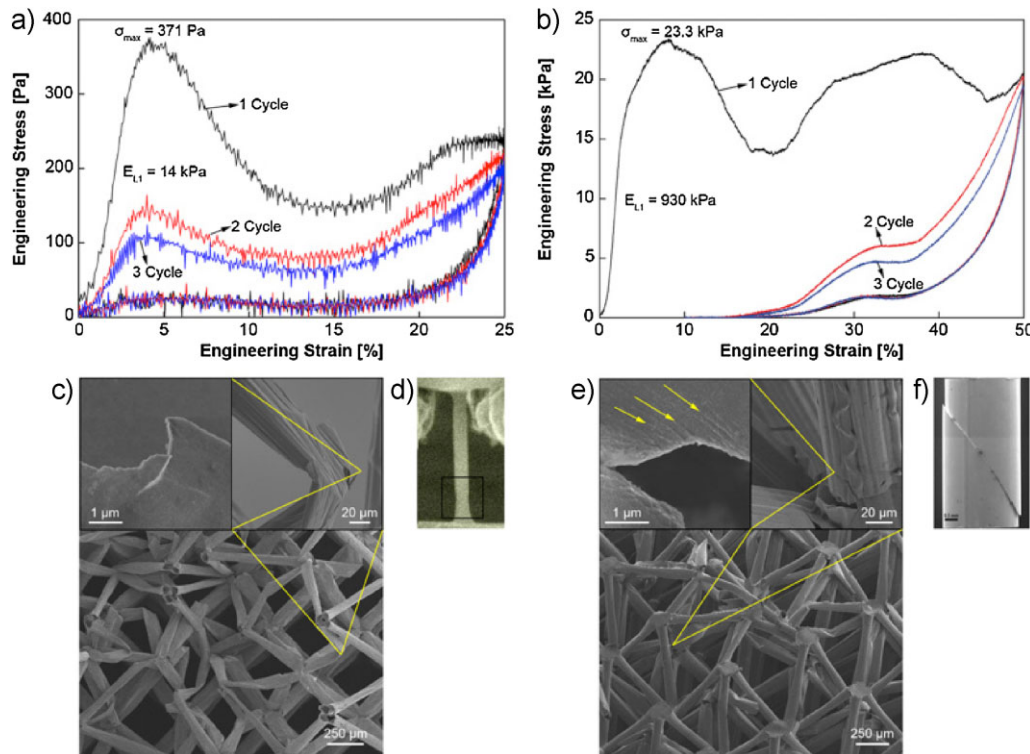


Fig. 3. Compression responses and post-mortem SEM images. (a) and (b) Quasi-static loading of microlattices with wall thicknesses of 85 nm (a) and 600 nm (b). (c) SEM image of a deformed microlattice with a wall thickness of 95 nm after three loading cycles. Plastic deformation is apparent up to high strains (inset right corner) with no evidence of shear banding (inset left corner) (d) Representative in situ SEM image of an amorphous NiP pillar with a diameter of 100 nm under tension, reprinted with permission from Ref.^[8] Necking is apparent (box). (e) SEM image of a deformed microlattice with a wall thickness of 600 nm after three loading cycles. The layers collapse with just little evidence of buckling events along the struts. Brittle fracture can be observed at the nodes (inset right corner), which is caused by shear banding and micro-crack propagation (inset left corner). (f) Representative metallic glass compression pillar, which collapsed along a single shear band.^[41]

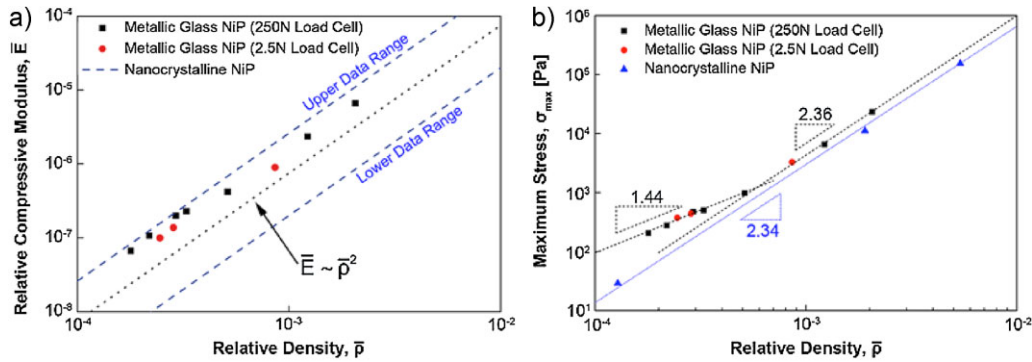


Fig. 4. Relative compressive modulus (a) and maximum attained strength (b) as a function of relative density. The black squares represent the samples measured with a 250 N load cell the red circles were measured using a 2.5 N load cell. The blue dashed data range in (a) and the blue triangles in (b) are samples with a nanocrystalline microstructure.^[43] (a) The relative modulus scales quadratically with the relative density, which is typical for stochastic open-cellular foams.^[11] (b) The maximum strength exhibits a clear transition in scaling from 2.36 to 1.44 for metallic glass NiP samples. This enhancement in maximum strength can be attributed to the brittle-to-ductile transition of the constituent material below a critical wall size of ≈ 150 nm.

normalizing the Young's modulus measured from the slope of the stress-strain curve in the first loading cycle, E_{L1} , by the Young's modulus of the constituent amorphous NiP, E_s , measured using nanoindentation:

$$\bar{E} = \left(\frac{E_{L1}}{E_s} \right) \quad (1)$$

Using this methodology may lead to overestimating the relative modulus because the indentation modulus obtained through Oliver–Pharr analysis is commonly lower than the actual modulus.^[33] This stems, in part, from the Oliver–Pharr analysis not accounting for the material anisotropy, from the assumption that the initial unloading is elastic-only, and from certain assumptions about the Poisson's ratio. The relative density $\bar{\rho}$ was estimated by dividing the density of the hollow NiP microlattice ρ by the density of the constituent solid ρ_s .^[20]

$$\bar{\rho} = \left(\frac{\rho}{\rho_s} \right) \quad (2)$$

The plot in Figure 4a shows that \bar{E} scales with $\bar{\rho}^2$, a behavior characteristic of bending-dominated open-cell foams.^[11] Dashed lines, which represent the bounds for the Young's modulus reported for similar deformed nanocrystalline NiP microlattices in Schaedler *et al.*,^[14] are provided for comparison. It is apparent that the metallic glass NiP microlattices were on average a factor of ≈ 2 stiffer than the nanocrystalline NiP samples with similar architectures. This is not surprising because metallic glasses are generally stiffer than nanocrystalline metals because of their high elastic limit.^[34] The maximum attained compressive stress of the NiP metallic glass microlattices, σ_{max} , was found to follow a $\bar{\rho}^m$ scaling, where m is a parameter dictated by the deformation mode of the structure (Figure 4b). Two different regimes were apparent in the σ_{max} versus $\bar{\rho}$ data: (1) samples with a relative density above 0.5% (regime I) had a power law scaling $\sigma_{max} \sim \bar{\rho}^m$ with $m = 2.36$ and (2) samples whose relative density was below 0.5%

(regime II) had a slope m of 1.44. A similar plot for nanocrystalline NiP microlattices shows a constant scaling with $m = 2.34$ and is provided for comparison.

6. In Situ Unit Cell Compression Experiments

Compressions of individual unit cells were performed in In SEM (Nanomechanics, Inc.), an instrument also known as SEMentor, which is a custom-built in situ nanomechanical instrument.^[35] All in situ nanomechanical experiments were conducted at a constant prescribed displacement rate of $2 \mu\text{m s}^{-1}$. Figure 5 shows the load versus displacement data during the first loading–unloading cycle of a single 60 nm-thick unit cell (Figure 5a), together with the corresponding in situ SEM images before loading, at maximum loading and after unloading (Figure 5b–d) and of the deformed regions after unloading (Figure 5e–h). The unit cell loaded elastically during the first $35 \mu\text{m}$ of displacement, after which the material flowed plastically at a relatively constant load of $122 \mu\text{N}$, which corresponds to an applied stress (load/unit cell area) of 221 Pa. Post-elastic buckling first occurred at the nodes (Figure 5e and f) and was accompanied by small non-catastrophic fracture events at the locales that experience the highest strain, marked in Figure 5. The maximum load of $253 \mu\text{N}$, which corresponds to an applied stress of 459 Pa, was reached at a displacement of $196 \mu\text{m}$, where the entire structure started to fail by elastic buckling events in the individual strut centers (captured frames B through D in Figure 5). Subsequent loading caused plastic deformation around the buckling regions at the struts. The residual displacement of $\approx 85 \mu\text{m}$ suggests that the structure underwent significant plastic deformation located around the nodes and the buckled struts. Subsequent loading had an elastic region followed by an extended plateau at 25% of the maximum load, P_{max} , of the first loading cycle, which suggests that the entire structure was fully damaged during the first loading and all subsequent cycling only strained parts elastically around those damage regions.

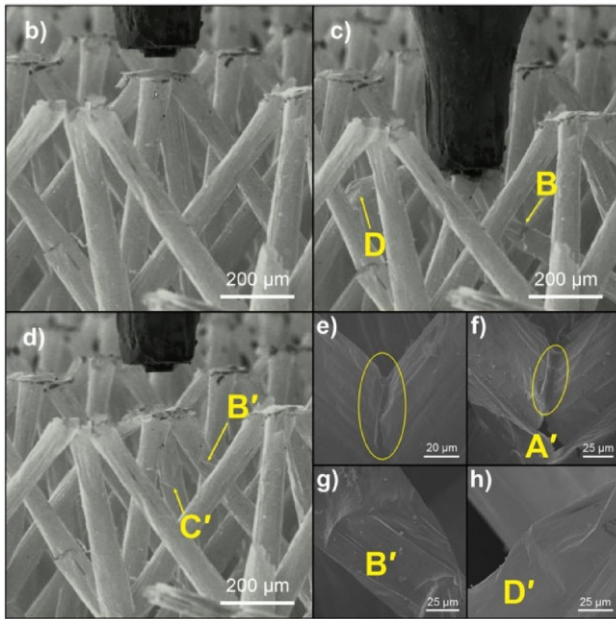
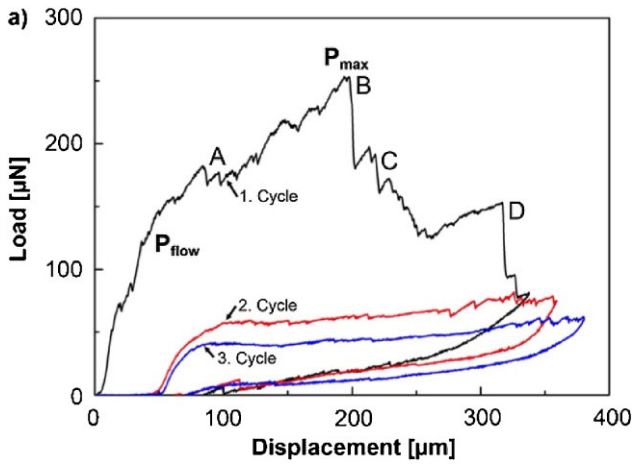


Fig. 5. Compressive response of a single unit cell with a wall thickness of 60 nm. (a) Load versus displacement curve of three loading–unloading cycle. Elastic deformation up to P_{flow} is followed by plastic deformation and micro-cracking at the nodes (A) as well as elastic buckling events at the struts (B–D) after reaching a maximum load P_{max} . (b–d) Snapshots of the in situ SEM movie taken before compression (b), at maximum compression (c), and after compression (d). (e and f) SEM images of the nodes after complete unloading of the structure. (g–h) SEM images of the unloaded plastic deformed buckling regions B and D.

7. Mechanical Modeling

We used simple analytical and numerical models to help elucidate the mechanical behavior of amorphous metal microlattices. All models were applied to the 65 nm-thick sample that was tested both at the lattice and at the unit-cell level. Closed-form expressions for yielding and buckling strength can be readily derived by analyzing the periodic deformation of a single unit cell loaded in compression.^[36] Each bar experienced a combination of axial, bending and shear loads. Yielding occurred when the maximum compressive stress in the bar near the node exceeded the yield strength of the material; buckling occurred when the same stress

exceeded the local buckling strength of a hollow tube under compression. The ratio of wall thickness to diameter in the micro-trusses, t/D , is much less than the ratio of the strut diameter to its length, D/L , which caused the local buckling to always precede Euler buckling for the geometry under consideration; additionally, yielding is not active, when $t/D \ll \sigma_y/E$ ^[36]. The effective lattice strength can then be expressed as^[36]:

$$\sigma_{\text{max}}^{\text{an}} = \frac{2\pi E(D/\ell)(t/\ell)^2}{\sqrt{3(1-\nu^2)\cos^3\theta(1+(D/\ell)\frac{\tan\theta}{2})}} \quad (3)$$

Applying Equation 3 to the samples described here, $\sigma_{\text{max}}^{\text{an}} = 280$ Pa. This simple analytical model predicts the onset of local buckling near the nodes but ignores the details of the nodal geometry. A more realistic estimate can be obtained with unit-cell-level Finite Elements simulations. A buckling analysis of a unit cell under axial compression, with all sides constrained from rotation and forced to remain planar (periodic boundary conditions allowing for Poisson's expansion) predicts a strength of $\sigma_{\text{max}}^{\text{FEM}} = 235$ Pa. This agrees well with the measured lattice-level strength of $\sigma_{\text{max}}^{\text{exp,lattice}} = 204$ Pa. In contrast to the amorphous Ni–P microlattices studied in this work, this type of FE simulations for nanocrystalline Ni–P micro-lattices overestimated the measured lattice strength by a factor of ≈ 3 – 5 .^[36] This discrepancy was attributed to premature nodal failure by partial fracture. To test this hypothesis, FE analyses were performed on unit cells with free edges, thus simulating the presence of cracks, and were found to agree with experimental results. For the lattice under consideration, a free-edge unit-cell simulation would predict a buckling strength as low as 75 Pa, well below experimental observations. The agreement between the experimental lattice-level strength and the periodic FE simulation results suggests that amorphous Ni–P microlattices with wall thickness < 100 nm are able to deform to appreciable strains, in contrast to the virtually non-existent deformability of nanocrystalline Ni–P lattices. More extensive simulations are being pursued to quantify the magnitude of this effect.

This analysis can also explain the observed difference between the compressive strength of a single unit-cell and that of the entire lattice. In the experiment performed on a single unit cell, the first deviation from linear elasticity occurred at 221 Pa due to a combination of local buckling, partial (non-catastrophic) fracture and localized yielding at the nodes. This is consistent with the FE buckling strength of 235 Pa associated with nodal buckling. In contrast to the multi-cell lattice, this phenomenon is not associated with the peak strength. The higher level of constraint from the rest of the (unloaded) lattice (Figure 5) combined with the stabilizing effect of the flat punch on the top node allowed further loading of the unit cell. Upon load increase, the cell rotated slightly, which induced bending stresses at the center of each bar; ultimately, a single bar buckled at the center, which was quickly followed by the remaining bars at an applied compressive stress of ≈ 459 Pa.

More extensive analyses are needed to fully unveil the deformation and failure mechanisms of amorphous metallic microlattices over a wide density range; the preliminary calculations presented here support the claim that ultra-thin-walled amorphous Ni–P lattices exhibit higher ductility than their nanocrystalline counterparts.

8. Discussion

Hollow metallic glass NiP microlattices were found to exhibit almost identical elastic properties to nanocrystalline NiP microlattices, as reported in Schaedler *et al.*^[14] The observed scaling of the relative modulus \bar{E} with the relative density $\bar{\rho}^2$ (Figure 4a) was found to be in agreement with the prediction by Gibson and Ashby^[11] for stochastic open cellular foams. This is not surprising because the structures studied here are bending dominated due to the chosen geometry and architecture. The enhancement in the relative Young's modulus by a factor ≈ 2 for the amorphous NiP structures can be explained in terms of different material properties: changing the microstructure from nanocrystalline ($\approx 7\%$ P) to amorphous ($\approx 13\%$ P) led to a reduction in the density from ≈ 8 to $\approx 7.8 \text{ kg m}^{-3}$, with the concomitant decrease in Young's modulus from 200 to 140 GPa.^[37]

The scaling of the maximum attained compressive stress σ_{max} was more complex (Figure 4b). It did not follow a constant slope, as might be expected for a constant failure mode for all samples. Two different regimes were observed: (i) Structures with wall thicknesses $>150 \text{ nm}$, corresponding to a relative density of 0.5%, had a power-law scaling close to $\sigma_{\text{max}} \sim \bar{\rho}^2$, consistent with the theoretical model describing buckling-dominated failure in open-cellular foams.^[11] The mechanism can be explained as follows: loading the sample beyond a critical load P_{crit} induced buckling at the nodes. The intrinsic brittle character of amorphous NiP at wall thicknesses above $\approx 150 \text{ nm}$ caused a rapid initiation and propagation of shear bands and micro-cracks immediately after loading to higher loads, which led to a final catastrophic failure of the entire sample. (ii) The scaling of $\bar{\rho}^2$ broke down for samples with wall thicknesses below this threshold size of $\approx 150 \text{ nm}$. This regime followed a scaling law close to $\sigma_{\text{max}} \sim \bar{\rho}^{1.5}$. The initial instability still occurred via buckling at the nodes. But instead of elastic-followed-by-catastrophic-failure behavior, the structure was able to absorb some of the strain-energy at the hinges and undergo plastic deformation because of the emergent ability of nano-sized metallic glasses to plastically deform at room temperature. In situ compression test of a single 60 nm thin unit cell confirmed this observation by demonstrating plastic deformation at the nodes and the localized buckling along the struts.

This transition from elastic-to-plastic failure can be explained by a material-induced size-effect and supports the reported brittle-to-ductile transition in nano-sized metallic glasses.^[8,9,12] The post-elastic deformation of metallic glasses is generally described as a collective atomistic motion of shear transformation zones (STZ), or clusters which contain 100

atoms.^[10] STZs, densely populated in a narrow region, can assemble into a large planar band referred to as a shear band.^[38,39] The critical stress at which the first shear band forms defines the yield stress of the metallic glass. Under uniaxial load metallic glasses often exhibit inhomogeneous plasticity at room temperature, which is caused by the coalescence of STZs into highly localized shear bands to accommodate the strain.^[40] Recently, homogeneous flow and enhanced plasticity were reported at room temperature in nano-sized metallic glass samples with dimensions of 100 nm and below.^[8,9,12] This size-dependent transition from a highly localized to a homogeneous flow is commonly referred as the brittle-to-ductile transition of metallic glasses.^[8] Although the underlying mechanism of this transition is still not fully elucidated, it is believed that by reducing the specimen size below a critical value shear banding gets suppressed since the propagation of an embryonic shear band is not the energetically favorable process anymore.^[8–10,13]

SEM images of deformed microlattices (Figure 3c and e) corroborated these observations even under complex loading conditions. Samples with thicker walls (Figure 3e) failed in a catastrophic fashion and had multiple, densely packed shear bands and micro-cracks around the fracture zones. This morphology is similar to that of a compressed Zr-based metallic glass micro-pillar, which collapsed along a single shear band (Figure 3f).^[41] Reducing the wall thickness below the threshold size enabled the structure to deform prior to failure, without any evidence of shear banding (Figure 3c). This dichotomy was observed in other sub-150 nm metallic glass structures.^[7–9,12,13] An example of one such nano-structure after tension is provided in Figure 3d,^[8] which shows that instead of catastrophic failure, here, deformation commenced via necking and homogeneous flow prior to final failure.

9. Summary and Conclusion

Hollow metallic glass NiP microlattices with the lowest densities of 0.2% and with the dimensions spanning from nanometers to microns, and even centimeters. Uniaxial compression experiments revealed a stress-strain signature characteristic for bending-dominated structures. Post-mortem morphology suggests that the initial instability and failure occurred via buckling for all measured relative densities. The metallic glass micro-lattices maximum compressive stress when their wall thickness was below a threshold size of $\approx 150 \text{ nm}$. This enhancement suggests the occurrence of different deformation mode and is therefore attributed to the transition from brittle-to-ductile in metallic glass NiP.^[7–9,12,13] Preliminary analytical and numerical models support this claim, although more extensive modeling and in situ experiments are needed to obtain a more comprehensive insight into the complex loading and transition conditions.

These findings highlight the crucial role of material-induced size effects in contributing to the overall structural strength

when the smallest characteristic dimensions are comparable with those of the material's microstructure.

Received: September 24, 2013

Final Version: November 18, 2013

-
- [1] L. J. Gibson, M. F. Ashby, *Cellular Solids: Structure and Properties*, Cambridge University Press, Cambridge **1999**.
- [2] H. N. G. Wadley, *Philos. Trans. A. Math. Phys. Eng. Sci.* **2006**, 364, 31.
- [3] N. A. Fleck, V. S. Deshpande, M. F. Ashby, *Proc. R. Soc. A Math. Phys. Eng. Sci.* **2010**, 466, 2495.
- [4] A. Öchsner, G. E. Murch, M. J. S. de Lemos, *Cellular and Porous Materials*. Wiley-VCH Verlag GmbH & Co. KGaA, Weinheim, Germany **2008**.
- [5] H. N. G. Wadley, *Adv. Eng. Mater.* **2002**, 4, 726.
- [6] A. J. Jacobsen, W. Barvosa-Carter, S. Nutt, *Adv. Mater.* **2007**, 19, 3892.
- [7] O. V. Kuzmin, Y. T. Pei, J. T. M. De Hosson, *Scr. Mater.* **2012**, 67, 344.
- [8] D. Jang, J. Greer, *Nat. Mater.* **2010**, 9, 215.
- [9] C. A. Volkert, A. Donohue, F. Spaepen, *J. Appl. Phys.* **2008**, 103, 083539.
- [10] C. Schuh, T. Hufnagel, U. Ramamurty, *Acta Mater.* **2007**, 55, 4067.
- [11] J. Schroers, *Adv. Mater.* **2010**, 22, 1566.
- [12] H. Guo, P. F. Yan, Y. B. Wang, J. Tan, Z. F. Zhang, M. L. Sui, E. Ma, *Nat. Mater.* **2007**, 6, 735.
- [13] J.-Y. Kim, D. Jang, J. R. Greer, *Adv. Funct. Mater.* **2011**, 21, 4550.
- [14] T. A. Schaedler, A. J. Jacobsen, A. Torrents, A. E. Sorensen, J. Lian, J. R. Greer, L. Valdevit, W. B. Carter, *Science* **2011**, 334, 962.
- [15] J. P. Marton, M. Schlesinger, *J. Electrochem. Soc.* **1968**, 115, 16.
- [16] K. H. Krishnan, S. John, K. N. Srinivasan, J. Praveen, M. Ganesan, P. M. Kavimani, *Metall. Mater. Trans. A* **2006**, 37, 1917.
- [17] Y. Jin, H. Yu, D. Yang, D. Sun, *Rare Met.* **2010**, 29, 401.
- [18] I. Baskaran, T. S. N. S. Narayanan, A. Stephen, *Mater. Chem. Phys.* **2006**, 99, 117.
- [19] A. Babanejad, M. Hashemi, Y. Rahmatallahpur, S. A. Nozad, *Bull. Mater. Sci.* **2012**, 35, 561.
- [20] G. Mallory, J. Hajdu, *Electroless Plating: Fundamentals and Application*. Noyes Publications/William Andrew Publishing, LLC, New York **1990**.
- [21] K. M. Gorbunova, A. A. Nikiforova, H. S. Myers, *J. Electrochem. Soc.* **1963**, 110, 160.
- [22] M. Calvo-Dahlborg, F. Machizaud, S. Nhien, B. Vigneron, U. Dahlborg, *Mater. Sci. Eng. A Struct. Mater. Prop. Microstruct. Process.* **1997**, 226, 197.
- [23] A. Révész, J. Lendvai, J. L. ránth, J. Pádár, I. Bakonyi, *J. Electrochem. Soc.* **2001**, 148, C715.
- [24] S. H. Park, D. N. Lee, *J. Mater. Sci.* **1988**, 23, 1643.
- [25] K.-H. Hur, J.-H. Jeong, D. N. Lee, *J. Mater. Sci.* **1990**, 25, 2573.
- [26] G. S. Cargill, *J. Appl. Phys.* **1970**, 41, 12.
- [27] S.-Y. Chang, Y. Lee, H. Hsiao, T. Chang, *Metall. Mater. Trans. A* **2006**, 37, 2939.
- [28] A. M. Pillai, a. Rajendra. a. K. Sharma, *J. Coat. Technol. Res.* **2012**, 9, 785.
- [29] M. R. VanLandingham, *J. Res. Natl. Inst. Stand. Technol.* **2003**, 108, 249.
- [30] W. C. Oliver, G. M. Pharr, *J. Mater. Res.* **2011**, 7, 1564.
- [31] J. R. Cahoon, W. H. Broughton, A. R. Kutzak, *Metall. Trans.* **1971**, 2, 1979.
- [32] D. Z. Chen, D. Jang, K. M. Guan, Q. An, W. a. Goddard, J. R. Greer, *Nano Lett.* **2013**, 13, 4462.
- [33] A. Oila, S. J. Bull, *Int. J. Mater. Res.* **2003**, 94, 793.
- [34] J. R. Trelewicz, C. a. Schuh, *Acta Mater.* **2007**, 55, 5948.
- [35] J.-Y. Kim, J. R. Greer, *Acta Mater.* **2009**, 57, 5245.
- [36] L. Valdevit, S. W. Godfrey, T. A. Schaedler, A. J. Jacobsen, W. B. Carter, *J. Mater. Res.* **2013**, 28, 2461.
- [37] M. Schlesinger, in *Mod. Electroplat.* (Eds: M. Schlesinger, M. Paunovic), John Wiley & Sons, Inc, Hoboken, NJ, USA **2010**.
- [38] A. Argon, H. Kuo, *Mater. Sci. Eng.* **1979**, 39, 101.
- [39] M. Falk, *Phys. Rev. B* **1999**, 60, 7062.
- [40] H. Kimura, T. Masumoto, *Acta Metall.* **1983**, 31, 231.
- [41] R. Maaß, D. Klaumünzer, J. F. Löffler, *Acta Mater.* **2011**, 59, 3205.
- [42] P. Dechkrong, S. Jiwajinda, P. Dokchan, M. Kongtungmon, N. Chomsaeng, T. Chairuangri, C.-C. Yu, C.-N. Hsiao, M. Shiojiri, *J. Struct. Biol.* **2011**, 176, 75.
- [43] A. Torrents, T. A. Schaedler, A. J. Jacobsen, W. B. Carter, L. Valdevit, *Acta Mater.* **2012**, 60, 3511.
-